Original Article

Fast Inversion Approach for Modeling Gravity Data: Varying Synthetic and Real Cases

Khalid S. Essa[1], Mahmoud Elhussein [1] and Omar A. Gomaa[1*]

[1] *Department of Geophysics, Faculty of Science, Cairo University, P.O. 12613, Giza, Egypt.*

ARTICLE INFO

ABSTRACT

Defining the causative source parameters is an essential tool in geophysical exploration and is often carried out using gravity subject datasets. Naturally stimulated metaheuristic optimization algorithms are primarily based totally on a few stochastic approaches, and have attracted greater interest over the past decade, because of their functionality to discover the finest answer of the version parameters from the explored area. This is done after making use of the distinct horizontal derivative orders at the located information, to lessen the local impacts. The most desirable management parameters of the particle swarm optimization rules were decided, using few parameters tuning research on artificial anomalies. The option for the optimization issues advanced with the aid of using the horizontal derivatives on the observed gravity data. So, the present-day inversion algorithm uses the third horizontal derivative, to minimize the regional anomaly and the particle swarm optimization, to estimate the different source model parameters. The present-day inversion algorithm was carried out on three different synthetic models (a two-sided dipping fault version with second and third orders regional, and without and with 5% and 10% random noises, a two-sided dipping fault with a - sphere shape model, without and with 5% and 10% random noises, and a -sided dipping fault model, without and with 10% random noises) and an actual field data set (from the USA). Applications have proven that, the present-day inversion algorithm provided close results. However, it indicates that, applying the higher horizontal derivatives turned into greater power in decreasing the regional component. The acquired results declared that, the present-day inversion algorithm works nicely, even with inside the existence of noises.

* Corresponding author at: *Department of Geophysics, Faculty of Science, Cairo University, P.O. 12613, Giza, Egypt.*
Email: omargomaa@cu.edu.eg

1. Introduction

Gravity inversion methods have proven to be a powerful tool in geophysics, providing insight into the subsurface density structure and helping to solve various exploration problems. These methods have been widely used in oil and gas exploration, mineral exploration, cavity finding, archeological site exploration, geothermal investigation, basin configuration and structures of the subsurface. (Panisova and Pasteka, 2009; Araffa et al., 2015; Bouhlassa et al., 2017; Uwiduhaye et al., 2018; Rezaie, 2019; Al-Farhan et al., 2019; Essa et al., 2020; Kumar et al., 2020; Essa and G´eraud, 2020; and Abedi, 2020) However, despite the success of these methods, they are not without limitations. (Tarantola, 2005) In particular, the inversion of the gravity data can be nonunique, making the inverse problem a poor setting.

The researchers worked hard to create and modify various techniques, to address these limitations and interpret fault-generated gravity data. These methods can be divided into two classifications: Some rely on simple geometrical models, and some use more complexes models. Simple geometrical models, such as graphic and mathematical methods, are often used to model buried structures and mainly focus on determining characteristic parameters of dipping faults. However, these approaches can be viewed as a limitation. Therefore, researchers have modified techniques, that consider more complex geometry models to overcome these limitations.

One such method is the method developed by Essa (2013) that based on the variance analysis. This method can simultaneously calculate the dip of the fault and the depth to the center of the fault upthrown plane from the horizontal derivatives of the residual gravity anomaly. However, this method has limitations: valid only if the regional gravity anomaly is represented by up to a first-order polynomial. Furthermore, the accuracy of the results depends on the accuracy, to which the origin of the fault is determined from the observed gravity data, and it does not consider the effect of the downthrown plane of the fault model.

Another method is the least-squares method developed by Abdelrahman and Essa (2015), which can successively estimate the dip value in degrees of the fault model, the depth to the upthrown plane of a thin fault and the amplitude coefficient, using the moving-average residual gravity anomalies. This method can overcome some of the limitations of the previous method, but it also has limitations.

Nowadays, there are many methods have been developed, based on artificial intelligence (AI). As genetic algorithm (Montesinos, et al., 2005; and Di Maio, et al., 2020), the (DE) differential evolution algorithm (Ekinci, et al., 2016; and Balkaya, et al., 2017), the gravitational search algorithm (Rashedi, et al., 2009), the dolphin echolocation (Kaveh and Faroudi, 2013), the ant colony optimization (ACO) algorithm (Dorigo and Stützle 2003), the simulated annealing algorithm (SA) (Biswas, 2015), the particle swarm optimization (PSO) algorithm (Essa, 2021; Essa, et al., 2021b; and Essa, et al., 2022) Those algorithms are not unusualplace amongst researchers, due to their versatility and advanced cappotential to cope with a style of problems.

This paper proposes a new approach to interpret the gravity data generated by faults. It is based on using the third horizontal derivative, through graticule spacing and applying the Particle Swarm Optimization (PSO) algorithm on evaluated anomalies from horizontal derivatives. This paper aims to improve the accuracy of gravity inversion results, by taking into account more complex geometry models and overcoming the limitations of

previous methods. The paper will discuss the results of applying this new approach to real-world data and will provide a comparison to the results obtained, using the traditional methods.

2. Methodology:
2.1. Forward modeling

Figure (1) shows the two-sided (normal or reverse) fault with the parameters (z_{up} is depth to the middle of the upthrown side, z_{down} is depth to the middle of the downthrown side of the fault, x_o indicates the location of the fault on the surface, x_i is the location of the observation points, Θ is the angle of the fault in degrees, M is the amplitude coefficient calculated using the gravitational constant G, the density contrast $\Delta\rho$, and the thickness of the faulted side t)along the profile of gravity data, as given by the following equation (1) (Hinze et al., 2013):

$$g\left(x_i, x_o, z_{up}, z_{down}, M, \theta\right) = M\left[1 + \frac{1}{\pi}\tan^{-1}\left(\frac{(x_i - x_o)}{z_{up}} + \cot\theta\right) - \frac{1}{\pi}\tan^{-1}\left(\frac{(x_i - x_o)}{z_{down}}\right) + \cot\theta\right] \dots (1)$$
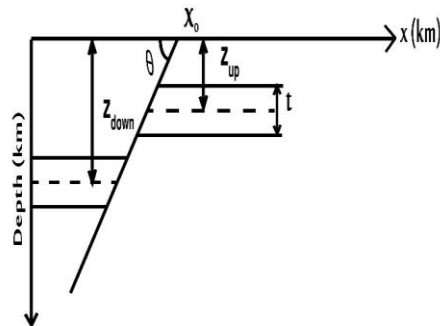

Fig. 1: A sketch, showing the parameters of a two-sided dipping fault structure.

2.2. Formulation of the inverse scheme

As a first step, the scheme starts by using the data generated, through the forward modeling in a synthetic example or by digitizing the data for the actual data set. Then, applying the third horizontal derivative technique, which was considered pioneering in separating the regional anomaly from the observed gravity data along the profile.

Essa and Munschy (2019) described the first horizontal derivative by the following equation:

$$\Delta g_x(x_i, s) = \frac{g(x_i + s) - g(x_i - s)}{2s} \dots\dots (2)$$

The third horizontal derivative of the different s values is called the graticule spacing, as the following equation can be used to separate the regional anomaly from the original total data (Darmawan, et al., 2019).

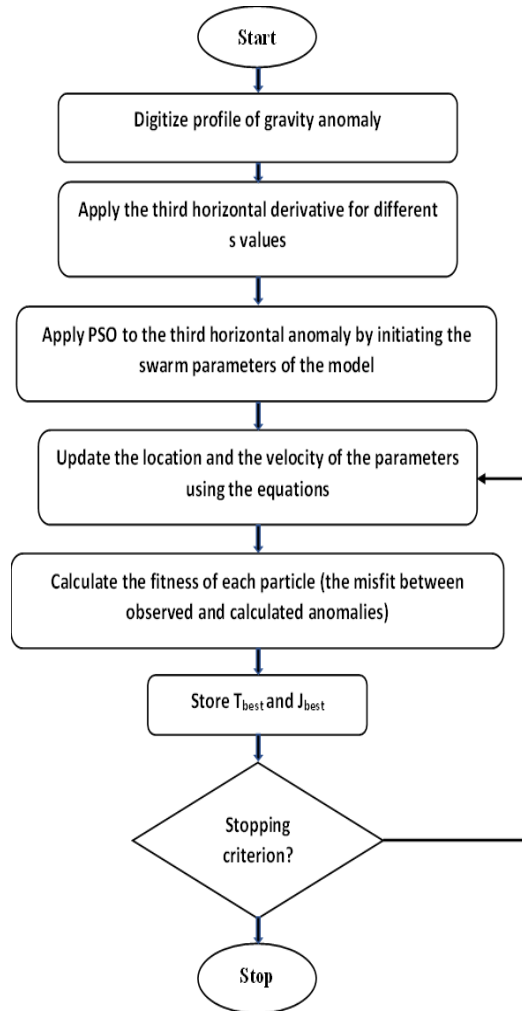$$\Delta g_{xxx}(x_i, s) = \frac{g(x_i+3s)-3g(x_i)+3g(x_i)-g(x_i-3s)}{8s^3} \dots (3)$$

```
                              Start

                    Digitize profile of gravity anomaly

              Apply the third horizontal derivative for different
                              s values

              Apply PSO to the third horizontal anomaly by initiating the
                      swarm parameters of the model

              Update the location and the velocity of the parameters
                          using the equations

              Calculate the fitness of each particle (the misfit between
                      observed and calculated anomalies)

                      Store T_best and J_best

                          Stopping
                          criterion?

                              Stop
```

Fig. 2: A flowchart, illustrating the model parameters estimation of the presented method.

2.3. The particle swarm optimization

Recent trends use evolutionary, stochastic heuristic and nature-inspired algorithms, to deal with non-linear problems. Nature-inspired algorithms, such as differential evolution, particle swarm optimization, cuckoo search and firefly algorithms are simple, flexible and efficient in solving many real-world problems.

In this paper, the applied algorithm is the particle swarm optimization, that established by Eberhart and Kennedy (1995). Inspired by the bird's search for natural food, the birds presented particles, that work in the search field to find the solution. Each particle has a random position and velocity vector. The location vectors are the parameter values. This technique has been applied to geophysical problems (Singh and Biswas, 2016; and Karcıoˇglu and Gürer, 2019). The random particles initiate the swarm and search for sources by describing

generations. During each iteration of the process, all of the particles upgrade their velocity and location, using the following formulas:

$$v_j^{L+1} = c_3 v_j^L + c_1 rand \left(T_{best} - x_j^{L+1}\right) + c_2 rand (J_{best} - x_j^{L+1})$$

$$x_j^{L+1} = x_j^L + v_j^{L+1}$$

where: x_j^L is the present location of the jth particles at the Lth iterations, v_j^L is the velocity of the jth particles at the Lth iterations, a random number between [0 and 1] has been used, through utilizing the rand function, the cognitive, the social and the inertial weight, that are the controlling parameters of the convergence of the particles, respectively represented by the three symbols c1, c2 and c3(Parsopoulos and Vrahatis, 2002). The parameter c_1 contributes towards the self-exploration of a particle; c_2 is the social parameter, which contributes towards the motion of the particles in a global direction; and c_3 is the inertial factor, that controls the velocity of each particle (Roshan and Singh, 2017).

Estimating the global minimum of the objective function (Жobjective) is the primary goal of using the particle swarm optimization (PSO) techniques, to estimate the model parameters of dipping fault, through the gravity data. (M, z$_{up}$, z$_{down}$, x$_o$, and Θ). The initial parameters of the model are incrementally updated, while the iterative process works to achieve the best fit of the observed and predicted gravity data.

To estimate the best model parameters using the following objective function (Жobjective):

$$Ж_{objective} = \sqrt{\frac{1}{u} \sum_{i=1}^{u} \left[\Delta g_j^{obs}(x_j) - \Delta g_j^{calc}(x_j)\right]^2}$$

where: u represent the observed data point numbers, Δg_j^{obs} represent the gravity data measurements, and Δg_j^{calc} represents the calculated gravity data at each data point x_j.

The flowchart of the procedures of estimating the model parameters represented in figure (2) following the incoming steps: The gravity data of the profile is read as the first step of the procedure, then applying the third horizontal derivatives as the second step, to reduce the effect of the regional data with different orders. Applying the code of the particle swarm optimization (PSO) will come, as a third step, to estimate the dipping fault parameter, which considers the best parameter of the fault. In contrast, the particles reach the global minimum by updating their velocity and location for each parameter. Using a wide range of iterations and different values of the population of birds or, as indicated here, as the number of particles increase, it takes much longer to estimate the best global solution. It keeps different answers until reaching the stable area, as the iteration number increase and finally applying the calculated parameters, using the forward model, to see the match between the observed and calculated gravity anomalies.

Figure (2). A flowchart of the procedures for estimating the two-sided fault model parameters. These four steps are: First, read the gravity data profile. Second, applying the third horizontal derivative with various window lengths (different s values), to minimize the effect of the regional background anomaly, and third using the horizontal derivative anomalies to estimate the best-buried fault parameters by applying the PSO algorithm. This updates the location and velocity of each particle, until the best global solution is reached. Following that, we

take the average of the best-calculated values of the parameters for each s window length. Fourth, forward modeling the estimated model parameters, to calculate the matching between the calculated and observed anomalies, to get the minimum root mean square. This indicates a better solution and parameters values, as shown in the objective function equation.

2.4. Synthetic models
2.4.1. Model no. 1: influence of a two-sided fault, with different orders of regional anomaly model

The examination of the accuracy of the algorithm, when it is applied to a model with interfering structures, a 100 km gravity data profile was generated; a two-sided fault model was generated. This profile (the amplitude coefficient M = 200 mGal, the depth to the middle of the upthrown plane z_{up} = 2 km, the dip angle value θ = 34°, the depth to the middle of the downthrown plane z_{down} = 4 km and the origin of the fault x_0 = 50 km) and at the first case, adding a second order regional, without and with 5%, and 10% random noises.
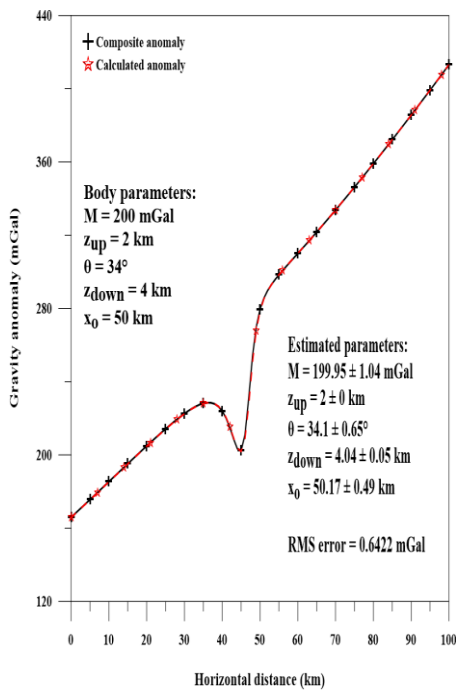

Fig 3: The composite gravity anomaly of a two-sided fault model and a deep-seated second-order regional structure. The calculated anomaly, by applying the third horizontal derivative, is also shown.
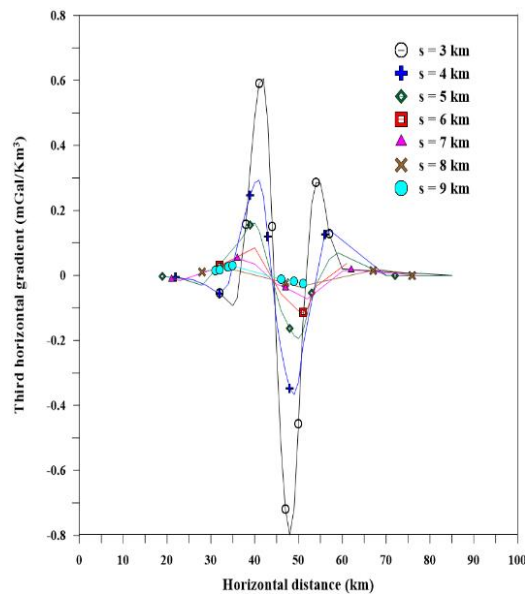
Fig.3a: The third horizontal derivative anomalies, using different s values of Fig (3), are shown.

The third horizontal derivative was applied to the gravity anomaly, using several s-values (s = 3:1:9 km) (Fig 3a); then, the PSO technique was applied to estimate the fault parameters. The estimated parameters are the amplitude coefficient M = 199.95 ± 1.04 mGal, the depth to the middle of the upthrown plane z_{up} = 2 ± 0 km, the dip angle value θ = 34.1 ± 0.65°, the depth to the middle of the downthrown plane z_{down} = 4.04 ± 0.05 km, the origin of the fault x_o = 50.17 ± 0.49 km and the root mean square of the error = 0.6422 mGal, in the case of free

noise model. Fig (3) shows the observed and predicted parameters of the two-sided fault, by applying the PSO to the third horizontal derivatives anomalies (Table 1), and the predicted parameters are the amplitude coefficient $M = 200.84 \pm 3.58$ mGal, the depth to the middle of the upthrown plane $z_{up} = 2.06 \pm 0.18$ km, the dip angle value $\theta = 32.8 \pm 2.57^{\circ}$, the depth to the middle of the downthrown plane $z_{down} = 3.9 \pm 0.2$ km, the origin of the fault $x_o = 49.82 \pm 0.84$ km, and the root mean square of the error $= 4.0569$ mGal, in the case of adding 5% random noises, as shown in Fig (3b). Fig (3c) shows the third horizontal derivative anomaly with 5% random noises.

In the case of adding 10% random noises to the same model, Fig (3d) shows the predicted parameters are the amplitude coefficient $M = 196.03 \pm 1.22$ mGal, the depth to the middle of the upthrown plane $z_{up} = 2.06 \pm 0.29$ km, the dip angle value $\theta = 30.9 \pm 0.83^{\circ}$, the depth to the middle of the downthrown plane $z_{down} = 4.17 \pm 0.2$ km, the origin of the fault $x_o = 49.27 \pm 1.04$ km and the root mean square of the error $= 11.1592$ mGal, as shown in Table (1). Fig (3e) shows the horizontal derivative anomalies, after adding 10% random noises, using different s values.
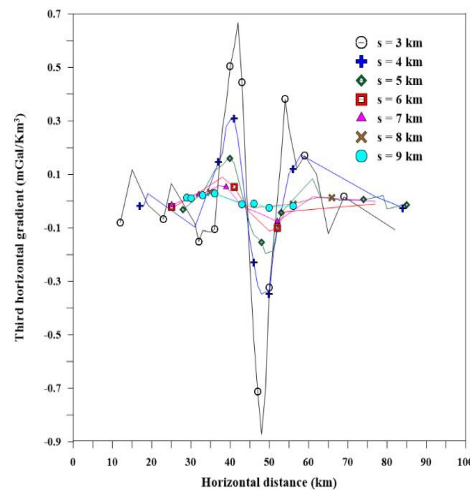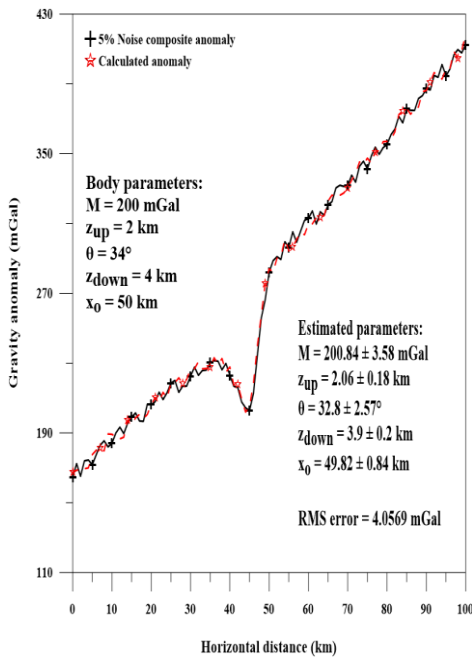

Fig. 3b: The composite gravity anomaly of a two-sided fault model and a deep-seated second-order regional structure, with 5% random noises. The calculated anomaly, by applying the third horizontal derivative, is also shown.

Fig. 3c: The third horizontal derivative anomalies, using different s values of Fig (3b). are shown.
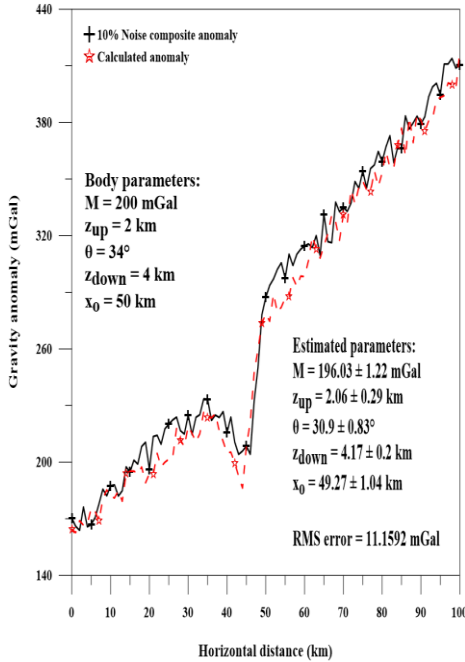
Figure 3d. The composite gravity anomaly of a two-sided fault model and a deep-seated second-order regional structure, with 10% random noises. The calculated anomaly, by applying the third horizontal derivative, is also shown.
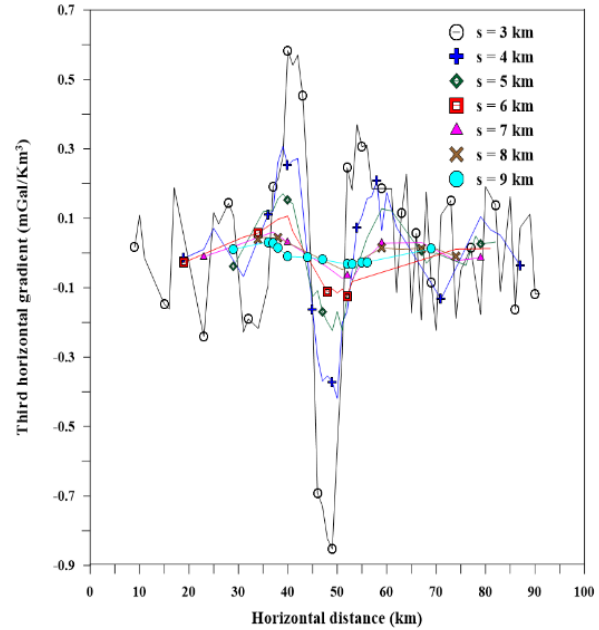

Figure 3e. The third horizontal derivative anomalies, using different s values of Fig (3d), are shown.

Adding a higher order of the regional anomaly, to test the presented scheme and its capability to deal with the third order regional anomaly, in the noise-free case and (5% & 10%) random noises level cases. Table (2) shows the estimated parameters, using the presented scheme, as follows in the noise-free, $M = 202.66 \pm 0.74$ mGal, $z_{up} = 2.07 \pm 0.11$ km, $\theta = 32.09 \pm 1.21°$, $z_{down} = 4.16 \pm 0.1$ km, $x_o = 49.47 \pm 0.79$ km and the root mean square of the error $= 4.0955$ mGal (Fig 4). Figure (4a) shows the third horizontal anomaly of the previous model.

In the case of 5% random noises, the predicted parameters are $M = 203.07 \pm 3.76$ mGal, $z_{up} = 1.89 \pm 0.13$ km, $\theta = 36.01 \pm 1.21°$, $z_{down} = 3.76 \pm 0.09$ km, $x_o = 48.62 \pm 0.5$ km and the root mean square of the error $= 7.0464$ mGal as shown in Fig (4b). Figure (4c) shows the third horizontal derivative anomaly of the previous model in the case of 5% random noises.
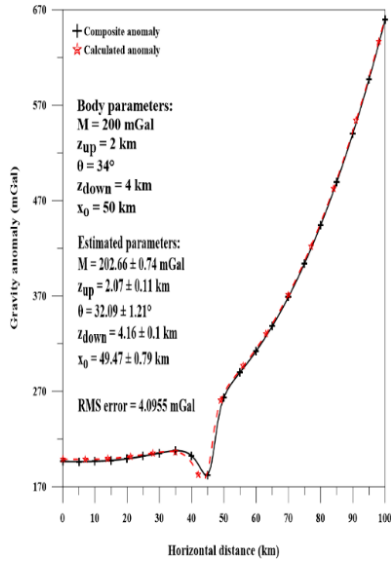
Figure 4. *The composite gravity anomaly of a two-sided fault model and a deep-seated third-order regional structure. The calculated anomaly, by applying the third horizontal derivative, is also shown.*

Figure 4a. The third horizontal derivative anomalies, using different s values of Fig (4). are shown.

Figure 4b. The composite gravity anomaly of a two-sided fault model and a deep-seated third-order regional structure, with 5% random noises. The calculated anomaly, by applying the third horizontal derivative, is also shown.

Figure 4c. The third horizontal derivative anomalies, using different s values of Fig (4b), are shown
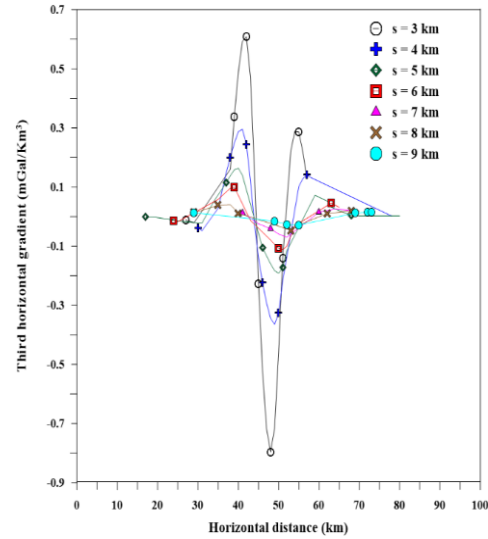
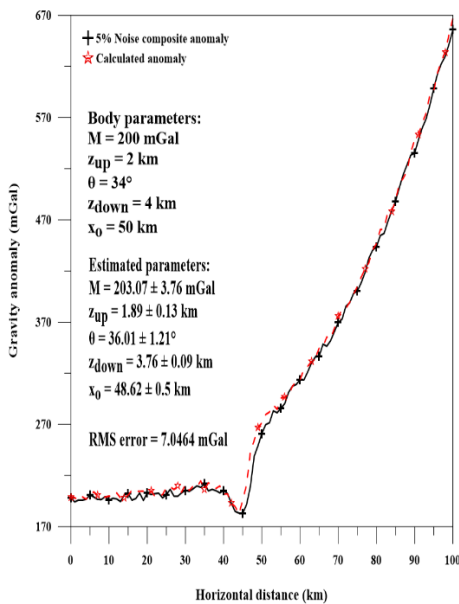*Figure 4e. The third horizontal derivative anomalies, using different s values of Fig (4d), are shown.*

Figure 4d. The composite gravity anomaly of a two-sided fault model and a deep-seated third-order regional structure, with 10% random noises. The calculated anomaly, by applying the third horizontal derivative, is also shown.
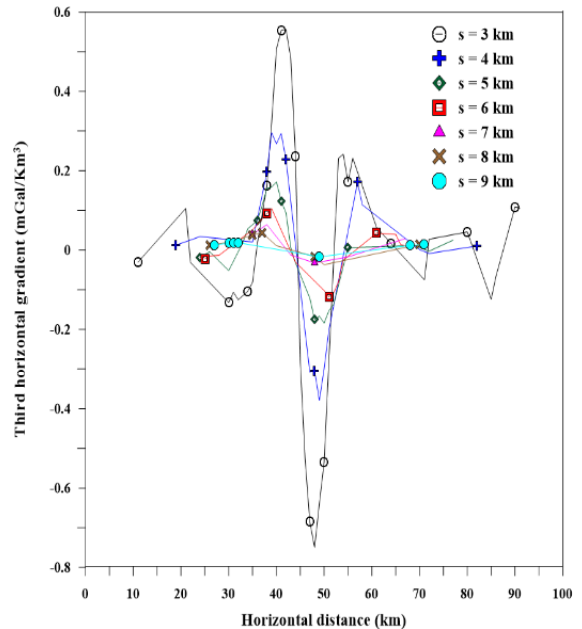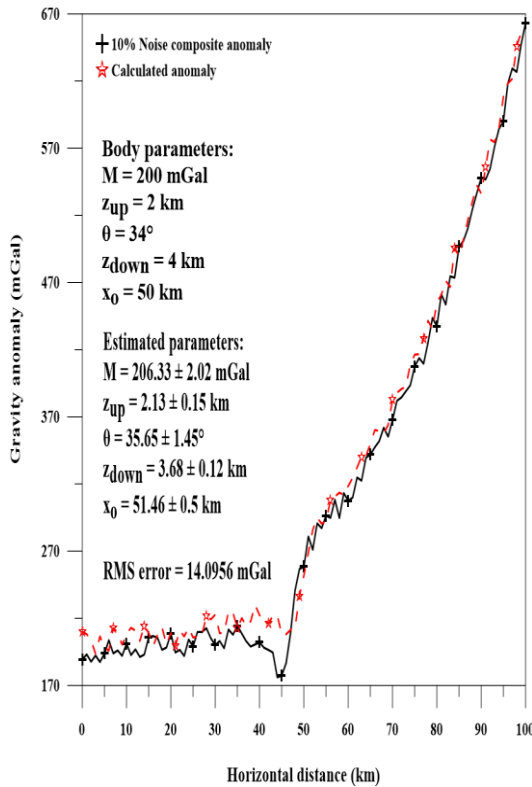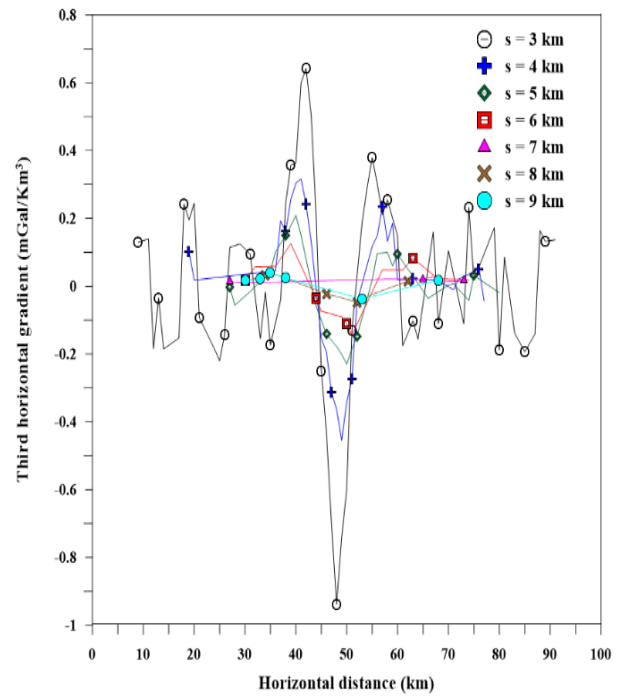
In the case of 10% random noises, the predicted parameters are M = 206.33 ± 2.02 mGal, z_{up} = 2.13 ± 0.15 km, θ = 35.65 ± 1.45°, z_{down} = 3.68 ± 0.12 km, x_o = 51.46 ± 0.5 km and the root mean square of the error = 14.0956 mGal, as shown in Fig (4d). Figure (4e) shows the third horizontal derivative anomaly of the previous model in the case of 10% random noises.

Model no. 2: influence of a two-sided fault, with two different spherical structures model

A two-sided fault model with the following parameters: (the amplitude coefficient M = 370 mGal, the depth to the middle of the upthrown plane z_{up} = 3 km, the dip angle value θ = 42°, the depth to the middle of the downthrown plane z_{down} = 5 km and the origin of the fault x_0 = 50 km) and two spherical structures with parameters as follows: (the depth to the middle of the first sphere z_1 = 4 km, the amplitude coefficient of the first sphere M_1 = 320 mGal, the depth to the middle of the second sphere z_2 = 2 km, the amplitude coefficient of the second sphere M_2 = 210 mGal, the location of the first sphere x_{O1} = 30 km and the location of the second sphere x_{O2} = 70 km) generates a gravity profile with a length of 100 km. The model was used, without and with 5% and

10% random noises. The third horizontal gradient was applied to the composite anomaly, using several s-values (s = 3:1:9 km) (Fig 5a). The PSO technique was applied to estimate the fault parameters. The estimated parameters are M = 369.99 ± 1.01 mGal, z_{up} = 3.02 ± 0.04 km, θ = 42.35 ± 1.02°, z_{down} = 4.99 ± 0.07 km, x_o = 50.09 ± 0.23 km and the root mean square of the error = 0.6350 mGal, in the case of free noise model.

Figure 5. The composite gravity anomaly of a two-sided fault model and two different spherical structures. The calculated anomaly, by applying the third horizontal derivative, is also shown.

Figure 5a. The third horizontal derivative anomalies, using different s values of Fig (5), are shown.

Fig (5) shows the observed and predicted parameters of the two-sided fault by applying the PSO to the third horizontal derivatives anomalies Table (3) in which the predicted parameters are M = 372.24 ± 2.92 mGal, z_{up} = 3.07 ± 0.09 km, θ = 43.01 ± 1.41°, z_{down} = 4.81 ± 0.17 km, x_o = 49.49 ± 0.22 km and the root mean square of the error = 7.6721 mGal, in the case of adding 5% random noises, as shown in Fig (5b). Fig (5c) represents the third horizontal derivative anomaly with 5% random noises. In the case of adding 10% random noises to the same model, Fig (5d) shows the predicted parameters are M = 377.3 ± 1.77 mGal, z_{up} = 2.81 ± 0.09 km, θ = 39.41 ± 0.94°, z_{down} = 4.78 ± 0.11 km, x_o = 50.87 ± 0.94 km and the root mean square of the error = 18.1373 mGal, as shown in Table (3). Fig (5e) represents the horizontal derivative anomalies after adding 10% random noises, using different s values.

Figure 5b. *The composite gravity anomaly of a two-sided fault model and two different spherical structures, with 5% random noises. The calculated anomaly, by applying the third horizontal derivative, is also shown.*
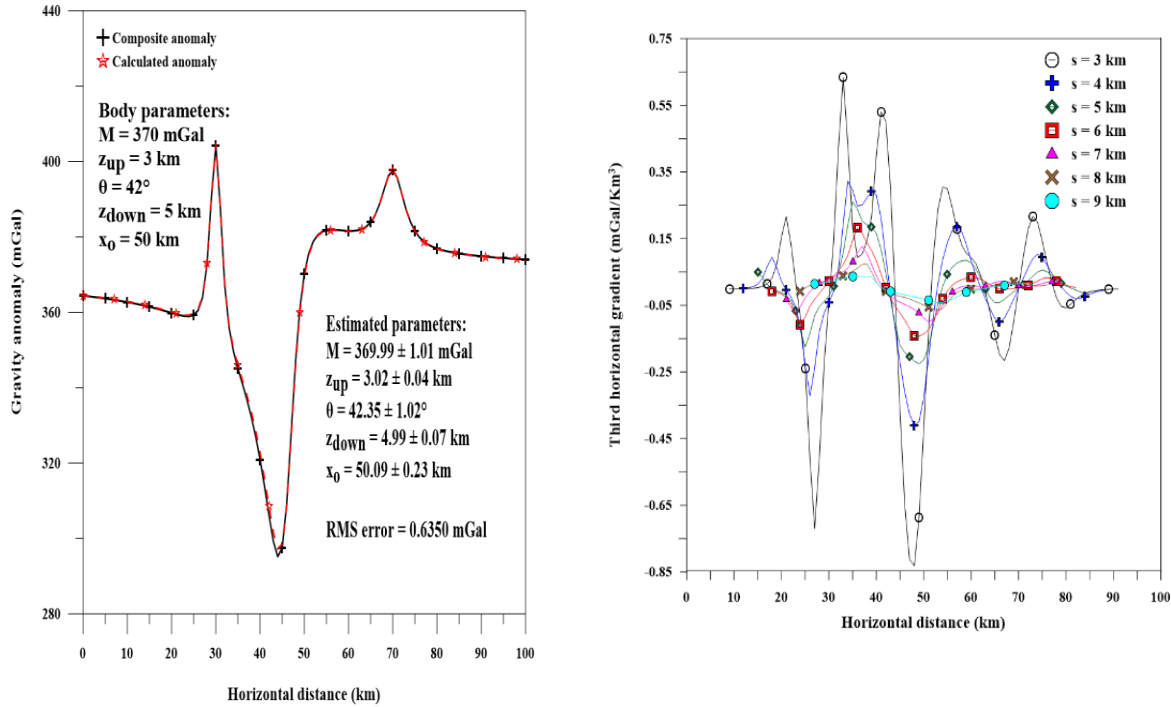

Figure 5c. *The third horizontal derivative anomalies, using different s values of Fig (5b), are shown.*
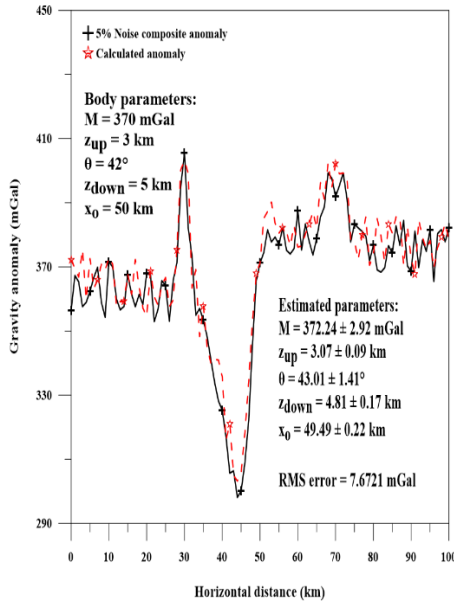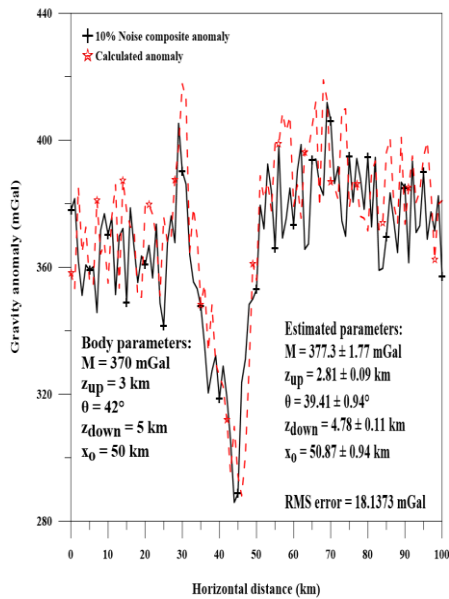

Figure 5d. *The composite gravity anomaly of a two-sided fault model and two different spherical structures, with 10% random noises. The calculated anomaly, by applying the third horizontal derivative, is also shown.*
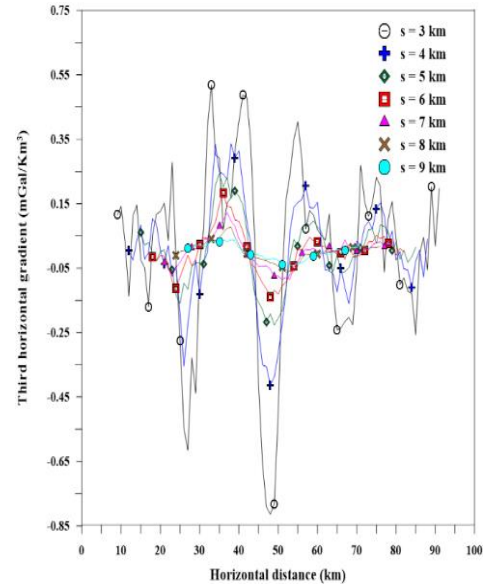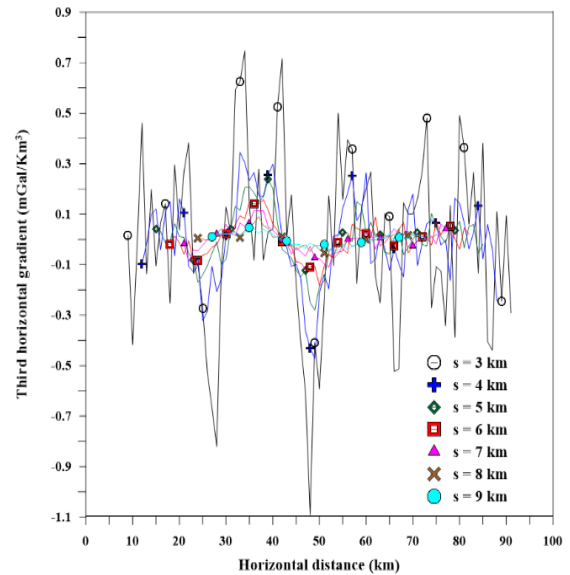

Figure 5e. *The third horizontal derivative anomalies, using different s values of Fig (5d), are shown.*

Model no.3: influence of two neighboring two-sided faults, without and with random noises

Two neighboring two-sided faults with different parameters: (the amplitude coefficient of the first fault M_1 = 410 mGal, the depth to the middle of the shared plane z_{sh} = 3 km, the dip angle of the first fault θ_1 = 55°, the depth to the middle of the upthrown plane of the first fault z_1 = 7 km, the origin of the first fault x_{o1} = 50 km)

Figure 6. The composite gravity anomaly of two neighboring two-sided fault models. The calculated anomaly, by applying the third horizontal derivative, is also shown.

and (the amplitude coefficient of the second fault M_2 = 460 mGal, the depth to the middle of the shared plane z_{sh} = 3 km, the dip angle of the second fault θ_2 = 30°, the depth to the middle of the upthrown plane of the second fault z_2 = 5 km, the origin of the second fault x_{o2} = 80 km) generates a gravity profile with a 140 km length Table (4). Fig (6) shows the observed and predicted parameters of the two neighboring faults without noises; in which the estimated parameters are (M_1 = 410.21± 1.4 mGal, z_{sh} = 2.99 ± 0.06 km, θ_1 = 55 ± 0.15°, z_1 = 7.06 ± 0.05 km, x_{o1} = 49.99 ± 0.01 km, M_2 = 462.45± 1.91 mGal, z_2 = 4.99 ± 0.06 km, θ_2 = 29.98 ± 0.09°, x_{o2} = 80 ± 0.01 km) and the root mean square = 2.6953 mGal.
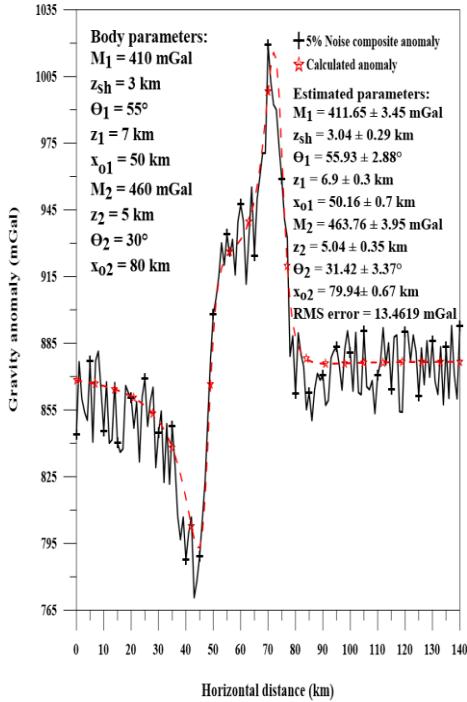
Figure 6a. *The composite gravity anomaly of two neighboring two-sided fault models. The calculated anomaly is also shown, by applying the third horizontal derivative, with 5% random noises.*
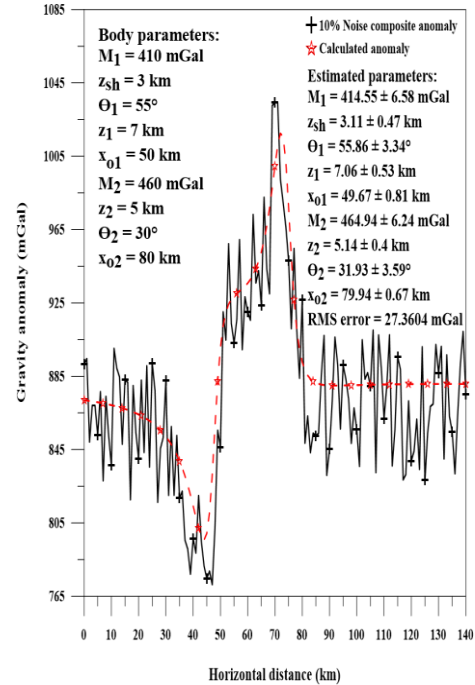
Figure 6b. *The composite gravity anomaly of two neighboring two-sided fault models. The calculated anomaly is also shown, by applying the third horizontal derivative, with 10% random noises.*

Fig (6a) shows the observed and predicted parameters by applying the PSO to the third horizontal derivative anomalies with 5% random noises ($M_1 = 411.65 \pm 3.45$ mGal, $z_{sh} = 3.04 \pm 0.29$ km, $\theta_1 = 55.93 \pm 2.88°$, $z_1 = 6.9 \pm 0.3$ km, $x_{o1} = 50.16 \pm 0.7$ km, $M_2 = 463.76 \pm 3.95$ mGal, $z_2 = 5.04 \pm 0.35$ km, $\theta_2 = 31.42 \pm 3.37°$, $x_{o2} = 79.94 \pm 0.67$ km) and the root mean square = 13.4619 mGal.

Fig (6b) shows the observed and predicted parameters by applying the PSO to the third horizontal derivative anomalies with 10% random noises ($M_1 = 414.55 \pm 6.58$ mGal, $z_{sh} = 3.11 \pm 0.47$ km, $\theta_1 = 55.86 \pm 3.34°$, $z_1 = 7.06 \pm 0.53$ km, $x_{o1} = 49.67 \pm 0.81$ km, $M_2 = 464.94 \pm 6.24$ mGal, $z_2 = 5.14 \pm 0.4$ km, $\theta_2 = 31.93 \pm 3.59°$, $x_{o2} = 79.94 \pm 0.67$ km) and the root mean square = 27.3604 mGal. Table (4). Figs. 6c, 6d and 6e show the third horizontal derivative anomalies using different s values (s= 2: 1: 10) without and with different levels of random noises, 5%, and 10%, respectively.

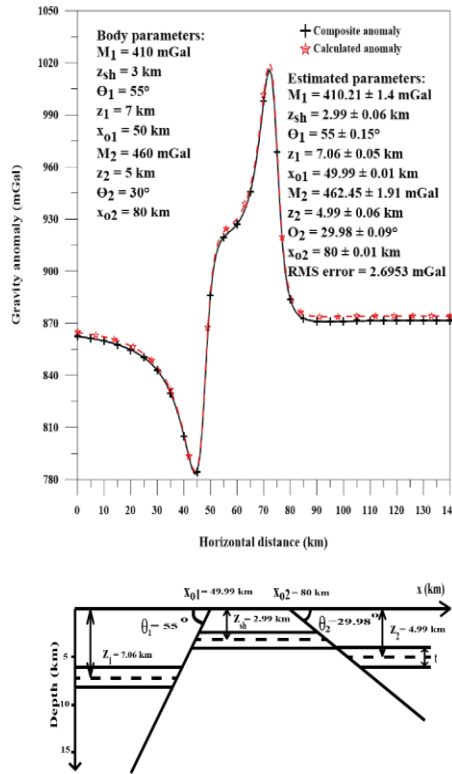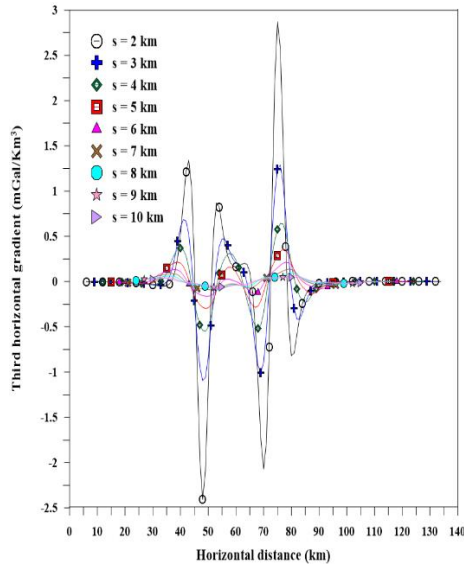*Figure 6c. The third horizontal derivative anomalies, using different s values of Fig (6), are shown.*

Figure 6d. The third horizontal derivative anomalies, using different s values of Fig (6a), are shown.
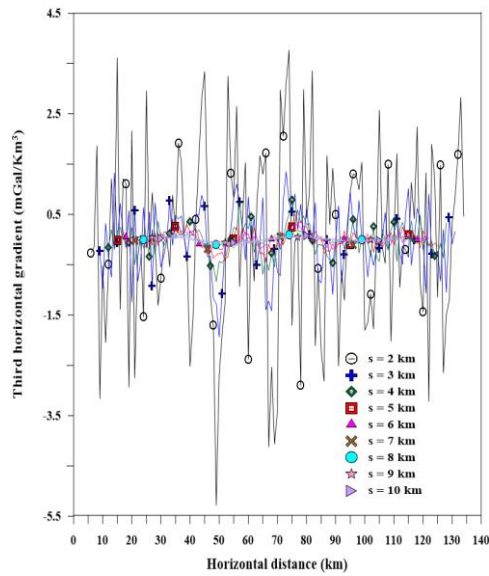
Figure 6e. The third horizontal derivative anomalies, using different s values of Fig (6b), are shown.

2.5. Real field examples

Real dataset: The Seattle fault system, Puget Lowlands, Western Washington, The USA

The algorithm has been examined formerly, using three different synthetic models without and with noises; the algorithm has been utilized on a real dataset, that was measured on the Seattle fault system, where The Puget Lowlands are located in the interior of the front region of the Cascadia Subduction Area. It is surrounded by the Cascade volcanic arc, the Old Mesozoic Terrane East and North, the Olympic Mountains and the Exhumed Accretion Complex West. The Puget Lowlands, at a depth of 25–30km, cover the Siletz Terrane, basalt and Island Arch rock composition (Simons and Crosson, 1997; and Brink, et al., 2002). The basement rocks below the settling basin reached 2.195–2.637 km deep (Rau and Johnson, 1999). These basement rocks are basalts interbedded with tuff, conglomerate, siltstone and mafic rocks, intercalated with sandstone (Brink, et al., 2002) (Fig 6).
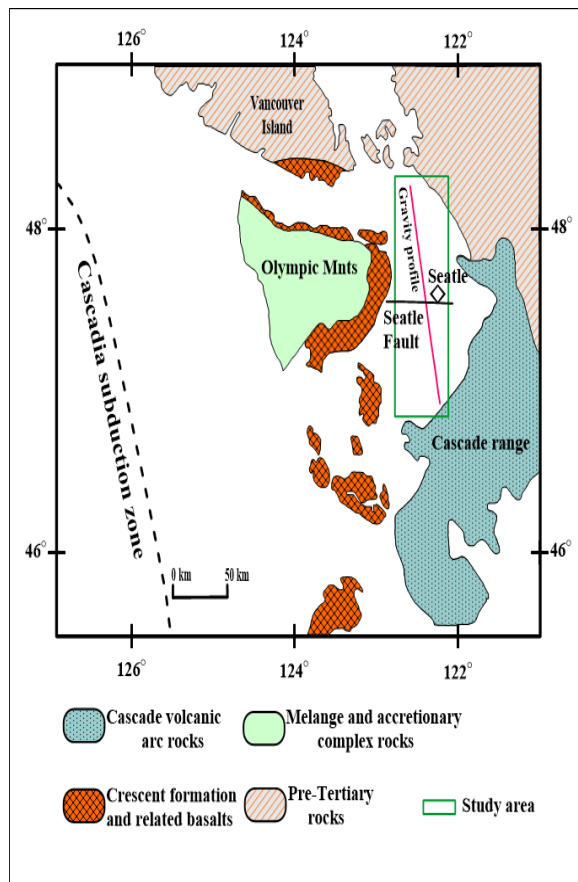
Figure 7. Real dataset: Geologic map (modified, after Brink, et al., 2002) of the Seattle fault system, Puget lowland, Western Washington, the United States of America.
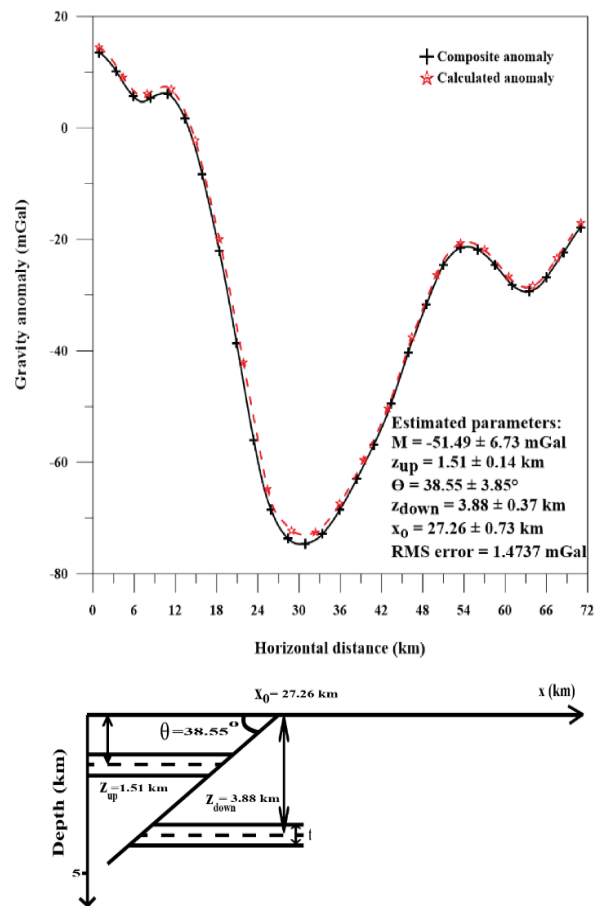
Figure 7a. Observed and predicted gravity data, by applying the current algorithm, are also shown.

Fig (7) represents the location of the measured gravity profile and the study area, which is nearly normal to the Seattle fault zone, which mainly consists of two steeply dipping layers deformed by two or more faults (Johnson, et al., 1994). The Seattle fault area is a reverse and thrust fault up to 7 km wide and over 70 km long, delimiting the north on edge of the Seattle uplift. It stands out, concerning its East–West orientation, depth to the bedrock and the hazard to an urban population center.
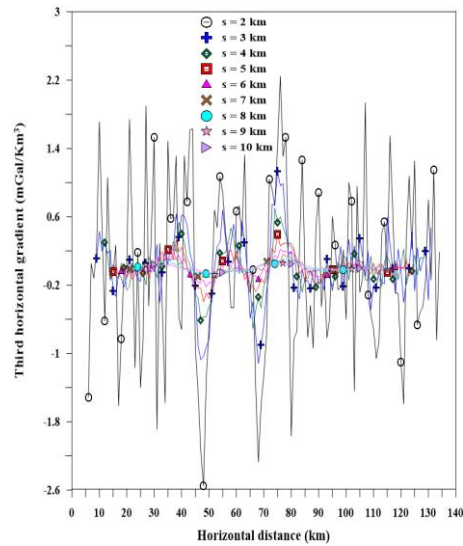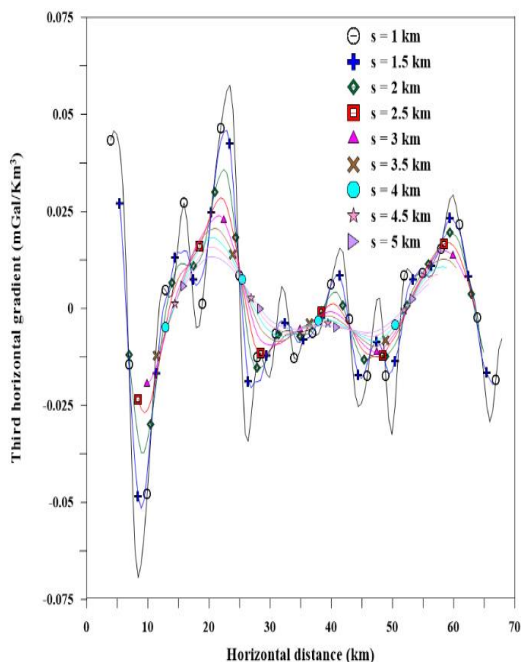

Figure 7b. The third horizontal derivative anomalies, using different s values of Fig (7a), are shown.
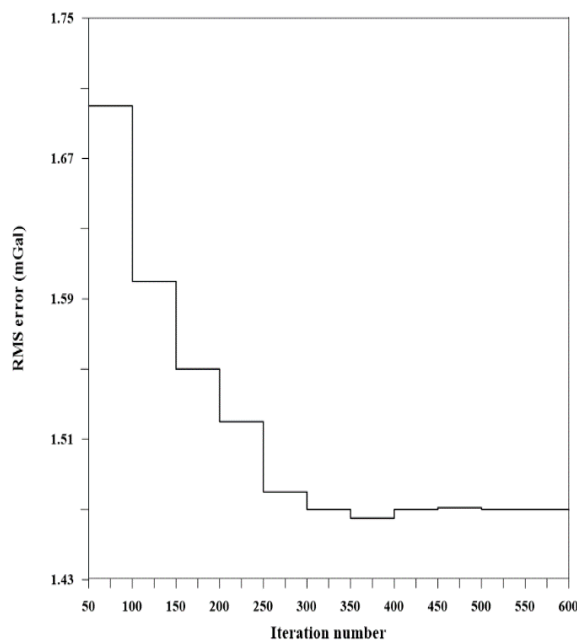
Figure 7c. The convergence rate of the particle swarm optimization, after applying the third horizontal derivatives.

Fig (7a) shows the estimated parameters by applying the PSO algorithm to the third horizontal derivative anomalies, using varying values of s (s = 1:0.5:5 km), as shown in Fig (7b). The estimated parameters are (the amplitude coefficient M = -51.49± 6.73 mGal, the depth to the middle of the upthrown plane z_{up} = 1.51 ± 0.1 km, the dip angle value in degrees θ = 38.55 ± 3.62°, the depth to the middle of the downthrown plane z_{down} = 3.88 ± 0.37 km, the origin of the fault x_o = 27.26 ± 0.87 km). The root mean square of the error = 1.47 mGal. Table (5). Fig (7c) shows the convergence rate of the PSO algorithm, using different iteration values.

Table (6) compares the previously published results and the present method result of the actual data set. It shows a close result and a good match with the geological model.

5. Conclusions

The current study, for the two-sided fault interpretation, uses the gravity data measured along a profile. This scheme depends upon the third horizontal derivative anomalies, to reduce the effect of the regional field data (calculated by using different values of s, to reduce the effect of the different polynomial orders of the regional data, up to the third polynomial order). Then, applying the PSO algorithm for estimating the parameters of the two-sided fault structure. The scheme has been applied to three synthetic models and a real example from the USA. It finds that, the scheme is stable, concerning noise levels and can estimate the parameters, with acceptable accuracy.

Author Contributions

Khalid S. Essa: Conceptualization, Methodology, Writing– original draft, Writing– review & editing. Anderson N. L: Writing– review & editing, Visualization. Omar A. Gomaa: Writing – review & editing, Visualization. Mahmoud Elhussein: Writing – review & editing, Visualization. All authors studied and accredited the final manuscript edit.

Table 1. Model no. 1: Results of the PSO-inversion algorithm applied to third horizontal derivative anomalies of the gravity profile (100 km) due to composite anomaly of two-sided dipping fault model (M = 200 mGal, z_{up} = 2 km, $\theta = 34°$, z_{down} = 4 km and x_0 = 50 km) and second order regional without and with 5%, 10% random noise.

Parameters	Used ranges	Results								Error (%)	RMS error (mGal)
		Noise-free case								
		s = 3 km	s = 4 km	s = 5 km	s = 6 km	s = 7 km	s = 8 km	s = 9 km	$\bar{\phi}$		
M (mGal)	-200 – 400	201	198	200.41	199.54	199.71	200	201	199.95± 1.04	0.0243	
z_{up} (km)	1 – 9	2	2	2	2	2	2	2	2±0	0	
θ (degree)	10 – 100	33.8	33.98	34	34.25	34.7	35	33	34.1± 0.65	0.3067	0.64
z_{down} (km)	1 – 10	4.1	4	4	4	4.1	4	4.1	4.04± 0.05	1.0714	
x_0 (km)	40 – 60	50	50	50	49.89	49.58	50.8	50.91	50.17± 0.49	0.3371	
		5% Random noise case								
M (mGal)	-200 – 400	397.11	384	396.62	400	395.06	397.14	394.06	396.34 ± 5.34	1.62	
z_{up} (km)	1 – 9	6.4	6.7	6.4	6.6	6.3	5.7	6.3	6.38 ± 0.29	6.30	
θ (degree)	10 – 100	37.12	44.06	35.74	36.12	44.25	43.54	45.74	41.84 ± 4.23	4.60	4.06
z_{down} (km)	1 – 10	9.6	9.3	8.7	8.8	9.5	9.4	8.7	9.19 ± 0.36	2.10	
x_0 (km)	40 – 60	69.02	69.36	69.65	71	69.49	69.51	70.87	70.09 ± 0.83	0.13	
		10% Random noise case								
M (mGal)	-200 – 400	397	381.67	379.71	382.03	384	385.3	381.7	383.2 ± 5.67	1.74	
z_{up} (km)	1 – 9	6.7	6.5	6.8	7.1	6.7	6.5	6.8	6.77 ± 0.19	12.78	
θ (degree)	10 – 100	44.74	45.05	46.04	47.1	47.43	46.57	46.15	45.98 ± 0.94	14.95	11.16
z_{down} (km)	1 – 10	8.6	8.5	8.6	8.2	8.3	8.4	8.7	8.47 ± 0.16	5.93	
x_0 (km)	40 – 60	72.05	71.89	72.41	73.09	71.55	71.3	72.79	72.12 ± 0.75	3.03	

Table 2. Model no. 1: Results of the PSO-inversion algorithm applied to third horizontal derivative anomalies of the gravity profile (100 km) due to composite anomaly of two-sided dipping fault model (M = 200 mGal, z_{up} = 2 km, θ = 34º, z_{down} = 4 km and x_0 = 50 km) and third order regional without and with 5%, 10% random noise.

Parameters	Used ranges	Results									
		Noise-free case									
		s = 3 km	s = 4 km	s = 5 km	s = 6 km	s = 7 km	s = 8 km	s = 9 km	φ	Error (%)	RMS error (mGal)
M (mGal)	-200 – 400	202.1	203	204.01	202	201.95	202.53	203	202.66± 0.74	1.3279	
z_{up} (km)	1 – 9	2.1	2.08	1.89	1.96	2.15	2.1	2.2	2.07± 0.11	3.4286	
θ (degree)	10 – 100	32.53	30.08	31.92	33.06	31.02	32.43	33.6	32.09± 1.21	5.6134	4.09
z_{down} (km)	1 – 10	4.1	4.18	4.07	4.2	4.24	4.3	4.02	4.16± 0.1	3.9643	
x_o (km)	40 – 60	48.58	48.96	50.53	50	50.33	49	48.91	49.47± 0.79	1.0543	
		5% Random noise case									
M (mGal)	-200 – 400	195	205	204.21	204.02	202.13	206.1	205	203.07± 3.76	1.5329	
z_{up} (km)	1 – 9	1.74	1.78	1.89	1.82	1.94	1.99	2.1	1.89± 0.13	5.2857	
θ (degree)	10 – 100	37.38	37.11	36.92	36.21	35.12	34.25	35.05	36.01± 1.21	5.8992	7.05
z_{down} (km)	1 – 10	3.77	3.8	3.69	3.63	3.7	3.91	3.8	3.76± 0.09	6.0714	
x_o (km)	40 – 60	48	48.05	48.63	49.25	49.07	49	48.35	48.62± 0.5	2.7571	
		10% Random noise case									
M (mGal)	-200 – 400	209.08	208	205.14	206	205.99	202.9	207.21	206.33± 2.02	3.1657	
z_{up} (km)	1 – 9	2.22	1.94	2.21	2.27	1.89	2.25	2.1	2.13± 0.15	6.2857	
θ (degree)	10 – 100	33.11	35.03	36.04	37.52	35.88	36.94	35.02	35.65± 1.45	4.8487	14.09
z_{down} (km)	1 – 10	3.52	3.83	3.61	3.56	3.81	3.73	3.72	3.68± 0.12	7.9286	
x_o (km)	40 – 60	52.01	51.39	50.91	51.05	51.84	50.99	52.04	51.46± 0.5	2.9229	

Table 3. Model no. 2: Results of the PSO-inversion algorithm applied to third horizontal derivative anomalies of the gravity profile (100 km) due to composite anomaly of two-sided dipping fault model (M = 370 mGal, z_{up} = 3 km, θ = 42°, z_{down} = 5 km and x_0 = 50 km) and two spherical structures with different amplitude coefficient, and at different depths as follow (z_1 = 4 km, M_1 = 320 mGal, z_2 = 2 km, M_2 = 210 mGal, x_{O1} = 30 km, and x_{O2} = 70 km) without and with 5%, 10% random noise.

Parameters	Used ranges	Results									
		Noise-free case									
		$s = 3$ km	$s = 4$ km	$s = 5$ km	$s = 6$ km	$s = 7$ km	$s = 8$ km	$s = 9$ km	ϕ	Error (%)	RMS error (mGal)
M (mGal)	100 – 800	371.02	369	368.31	370.05	370.5	371	370.04	369.99 ± 1.01	0.0031	
z_{up} (km)	1 – 8	3	3	3	3.09	3	3.07	3	3.02± 0.04	0.7619	
θ (degree)	10 – 120	41.27	41.88	41.02	43.88	42.66	42.71	43.05	42.35± 1.02	0.8401	0.64
z_{down} (km)	1 – 12	5.06	5.1	4.89	5	5	4.91	5	4.99± 0.07	0.1143	
x_0 (km)	40 – 60	50.04	50.39	50.44	49.79	50	50	50	50.09± 0.23	0.1886	
		5% Random noise case									
M (mGal)	100 – 800	375	375.07	368.08	368.44	372.07	373	374	372.24± 2.92	0.6046	
z_{up} (km)	1 – 8	3.05	3.2	3.14	2.94	2.99	3.06	3.1	3.07± 0.09	2.2857	
θ (degree)	10 – 120	42.85	43.41	41	41.55	43.06	44.07	45.11	43.01± 1.41	2.398	7.67
z_{down} (km)	1 – 12	4.6	4.72	4.9	4.8	4.7	4.81	5.12	4.81± 0.17	3.8571	
x_0 (km)	40 – 60	49.55	49.18	49.53	49.79	49.63	49.5	49.22	49.49± 0.22	1.0286	
		10% Random noise case									
M (mGal)	100 – 800	378.09	376.18	380.1	377.08	378.25	374.5	376.87	377.3± 1.77	1.9718	
z_{up} (km)	1 – 8	2.7	2.83	2.76	2.92	2.71	2.83	2.91	2.81± 0.09	6.381	
θ (degree)	10 – 120	39.07	40.01	40	40.5	37.8	38.66	39.81	39.41± 0.94	6.1735	18.14
z_{down} (km)	1 – 12	4.82	4.9	4.93	4.72	4.8	4.62	4.7	4.78± 0.11	4.3143	
x_0 (km)	40 – 60	50.56	50.99	51.02	51.64	52	49.05	50.82	50.87± 0.94	1.7371	

Table 4. Model no. 3: Results of the PSO-inversion algorithm applied to third horizontal derivative anomalies of the gravity profile (140 km) due to composite anomaly of two two-sided dipping fault models (M_1= 410 mGal, z_{sh}= 3 km, z_1= 7 km, $\theta_1 = 55°$) and (M_2= 460 mGal, z_{sh}= 3 km, z_1= 7 km, $\theta_1 = 55°$) without and with 10% random noise.

Parameters	Used ranges	Results												
		noise-free case											
		s = 2 km	s = 3 km	s = 4 km	s = 5 km	s = 6 km	s = 7 km	s = 8 km	s = 9 km	s = 10 km	ϕ	Error (%)	RMS error (mGal)
M_1 (mGal)	200 – 750	412.13	407.06	410	410	410	410	410.95	411.32	410.39	410.21± 1.4	0.05	
z_{sh} (km)	1 – 6	3	3	3.1	3	3	2.9	3	2.9	3	2.99± 0.06	0.37	
θ_1 (degree)	10 – 100	55.14	55.13	55	55	55	55	55.06	54.63	55	55± 0.15	0.01	
z_1 (km)	3 – 10	7	7	7.1	7.1	7.1	7.1	7	7.1	7	7.06± 0.05	0.79	
x_{o1} (km)	30 – 70	49.99	49.98	50	50	50	50	49.98	50	50	49.99± 0.01	0.01	2.70
x_{o2} (km)	60 – 100	80.01	80.03	79.99	80	80	80	80	80	80	80± 0.01	0.00	
θ_2 (degree)	10 – 100	29.92	29.77	30.06	30	30	30	30	30.01	30.02	29.98± 0.09	0.08	
M_2 (mGal)	100 – 600	463	464.05	462	465.05	461	463	464.21	459.33	460.39	462.45± 1.91	0.53	
z_2 (km)	2 – 8	5	5	5.1	5	4.9	5	5	4.9	5	4.99± 0.06	0.22	
		5 % Random noise case											
M_1 (mGal)	200 – 750	409	412	415	412.63	407	406.06	414.17	415	414	411.65± 3.45	0.4027	
z_{sh} (km)	1 – 6	2.7	3.3	3.4	2.8	3.3	3.2	3.2	2.7	2.8	3.04± 0.29	1.4815	
θ_1 (degree)	10 – 100	52.01	58.44	58.1	54	51	57	56.78	58.9	57.11	55.93± 2.88	1.6848	
z_1 (km)	3 – 10	7.2	7.3	6.7	6.8	7.2	6.6	7.1	6.5	6.7	6.9± 0.3	1.4286	
x_{o1} (km)	30 – 70	51	49.88	51	49.05	49.76	50.61	50.32	50.49	49.35	50.16± 0.7	0.3244	13.46
x_{o2} (km)	60 – 100	79	80.12	80.58	79.49	79.24	81	80.53	79.67	79.79	79.94± 0.67	0.0806	
θ_2 (degree)	10 – 100	33.31	34.56	27	28.07	26	34	33.47	33.39	33	31.42± 3.37	4.7407	
M_2 (mGal)	100 – 600	457.81	465.01	464.22	468	467.99	466.42	465	462	457.41	463.76± 3.95	0.8179	
z_2 (km)	2 – 8	4.7	4.7	5.3	5.4	4.6	5.4	5.3	5.3	4.7	5.04± 0.35	0.8889	
		10 % Random noise case											
M_1 (mGal)	200 – 750	414	415.26	417.88	418	403	419	421	404.05	418.74	414.55± 6.58	1.11	
z_{sh} (km)	1 – 6	2.6	2.6	3.5	3.4	2.7	2.6	3.5	3.7	3.4	3.11± 0.47	3.70	
θ_1 (degree)	10 – 100	58	56.04	59.99	50.74	50	57.95	57.01	57	56	55.86± 3.34	1.56	
z_1 (km)	3 – 10	6.5	7.5	7.6	7.4	6.6	6.5	7.5	7.5	6.4	7.06± 0.53	0.79	
x_{o1} (km)	30 – 70	50	49.03	49	51	49.04	49.31	49.2	51	49.44	49.67± 0.81	0.66	27.36
x_{o2} (km)	60 – 100	79	80.12	80.58	79.49	79.24	81	80.53	79.67	79.79	79.94± 0.67	0.08	
θ_2 (degree)	10 – 100	31.99	34.26	26.32	27.72	28.45	33.07	34	36.55	35	31.93± 3.59	6.43	
M_2 (mGal)	100 – 600	470	465.05	453.27	456.29	464	468	471	469.84	467	464.94± 6.24	1.07	
z_2 (km)	2 – 8	4.7	5.7	5.5	4.9	4.8	4.6	5.4	5.3	5.4	5.14± 0.4	2.89	

Table 5. Results of the PSO-inversion algorithm applied to the third horizontal derivative anomalies of the Seattle fault, Puget Lowland, western Washington, The United States of America.

| Parameters | Used ranges | Results | | | | | | | | | | RMS error (mGal) |
		$s = 1$ km	$s = 1.5$ km	$s = 2$ km	$s = 2.5$ km	$s = 3$ km	$s = 3.5$ km	$s = 4$ km	$s = 4.5$ km	$s = 5$ km	ϕ	
M (mGal)	-420 – 200	-47.02	-54.24	-46.74	-41.8	-58.91	-57.8	-60.99	-45.92	-50	-51.49± 6.73	
z_{up} (km)	0.4 – 6.5	1.5	1.59	1.61	1.59	1.5	1.45	1.28	1.5	1.6	1.51±0.1	
θ (degree)	10 – 90	37	34.08	42.33	40	38.07	45.13	39	37.34	34	38.55± 3.62	1.47
z_{down} (km)	0.5 – 8	3.6	3.7	4.3	3.6	3.4	3.8	4.2	4.5	3.8	3.88± 0.37	
x_0 (km)	25 – 35	26.9	25.8	27.3	28.4	28.4	26.7	26.5	27.6	27.7	27.26± 0.87	

Table 6. A comparison between previous published results and the present method of the Seattle fault, Puget Lowland, western Washington, The United States of America

| Parameters | Brink et al. (2002) method | Anderson et al. (2020) method | The present method |
			Applying PSO on the Third horizontal derivative
M (mGal)	-	-72.61 ± 15.74	-51.49 ± 6.73
z_{up} (km)	1.5	2.2 ± 0.52	1.51 ± 0.1
θ (degree)	40	-	38.55 ± 3.62
z_{down} (km)	3.8	-	3.88 ± 0.37
x_0 (km)	26.5	25.06 ± 0.97	27.26 ± 0.87

DECLARATIONS

Funding

Not applicable.

Conflicts of interest

The authors state that, they have no competing interests.

Data availability

The authors declare that, the data are available upon request.

References:

Abdelrahman, E.M., Essa, K.S. (2015). Three least-squares minimization approaches to interpret gravity data due to dipping faults. Pure Appl. Geophys. 172, pp. 427–438.

Abedi, M. (2020). A focused and constrained 2D inversion of potential field geophysical data through Delaunay triangulation, a case study for iron-bearing targeting at the Shavaz deposit in Iran. Phys. Earth Planet. Inter. 309, 106604.

Al-Farhan, M., Oskooi, B., Ardestani, V.E., Abedi, M., Al-Khalidy, A. (2019). Magnetic and gravity signatures of the Kifl oil field in Iraq. J. Pet. Sci. Eng. 183, 106397.

Anderson, N.L., Essa, K.S., Elhussein, M. (2020). A comparison study using particle swarm optimization inversion algorithm for gravity anomaly interpretation due to a 2D vertical fault structure. J. Appl. Geophys. 179, 104120.

Araffa, S. A. S., Sabet, H. S., & Gaweish, W. R. (2015). Integrated geophysical interpretation for delineating the structural elements and groundwater aquifers at central part of Sinai Peninsula Egypt. Journal of African Earth Sciences, 105, pp. 93–106.

Biswas, A. (2015). Interpretation of residual gravity anomaly caused by simple shaped bodies using very fast simulated annealing global optimization. Geosci. Front 6, pp. 875–893.

Bouhlassa, S., Fehdi, C., Boubaya, D. (2017). Application of microgravimetry to assessing collapse risk in carbonate sinkhole areas, Cheria Basin, Northeast. Algeria. J. Life Sci. 11, pp. 232–248.

Balkaya, C., Ekinci, Y. L., Gokturkler, G., & Turan, S. (2017). 3D non-linear inversion of magnetic anomalies caused by prismatic bodies using differential evolution algorithm. Journal of Applied Geophysics, 136, pp. 372–386.

Brink, U.S., Molzer, P.C., Fisher, M.A., Blakely, R.J., Bucknam, R.C., Parsons, T., Crosson, R.S., Creager, K.C. (2002). Subsurface geometry and evolution of the Seattle Fault zone and the Seattle Basin, Washington. Bull. Seismol. Soc. Am. 92 (5), pp. 1737–1753.

Di Maio, R., Milano, L., Piegari, E. (2020). Modeling of magnetic anomalies generated by simple geological structures through genetic-price inversion algorithm. Phys. Earth Planet. Inter. 305, 106520.

Dorigo, M., Stützle, T. (2003). The ant colony optimization metaheuristic: algorithms, applications, and advances. In: Glover, F., Kochenberger, G.A. (Eds.), Handbook of Metaheuristics., 57. International Series in Operations Research & Management Science, Springer, Boston, MA. https://doi.org/10.1007/0-306-48056-5_9

Darmawan, R.A.S., Sutomo, A.D., Legowo, B. (2019). Determination of optimal window in spectrum analysis process with moving average method gravity data measurement. J. Phys. Conf. Ser. 1153, 012027.

Eberhart, R.C., Kennedy, J. (1995). A new optimizer using particle swarm theory. In: Proceedings of the IEEE The SiXth Symposium on Micro Machine and Human Centre, Nagoya, Japan, pp. 39–43.

Ekinci, Y.L., Balakaya, C., Gokturkler, G., Turan, S. (2016). Model parameter estimations from residual gravity anomalies due to simple-shaped sources using Differential Evolution Algorithm. J. Appl. Geophys 129, pp. 133–147.

Essa, K.S., G´eraud, Y. (2020). Parameters estimation from the gravity anomaly caused by the two-dimensional horizontal thin sheet applying the global particle swarm algorithm. J. Pet. Sci. Eng. 193, 107421.

Essa, K.S., Mehanee, S.A., Soliman, K.S., Diab, Z.A. (2020). Gravity profile interpretation using the R-parameter imaging technique with application to ore exploration. Ore Geol. Rev. 126, 103695.

Essa, K.S. (2013). Gravity interpretation of dipping faults using the variance analysis method. J. Geophys. Eng. 10, 015003.

Essa, K.S. (2021). Evaluation of the parameters of fault-like geologic structure from the gravity anomalies applying the particle swarm. Environ. Earth Sci. 80, 489.

Essa, K.S., G´eraud, Y., Diraison, M. (2021b). Fault parameters assessment from the gravity data profiles using the global particle swarm optimization. J. Pet. Sci. Eng. 207, 109129.

Essa, K.S., Abo-Ezz, E.R., G´eraud, Y., Diraison, M. (2022). A full interpretation applying a metaheuristic particle swarm for gravity data of an active mud diaper, SW Taiwan. J. Pet. Sci. Eng. 215, 110683.

Essa, K.S., Munschy, M. (2019). Gravity data interpretation using the particle swarm optimization method with application to mineral exploration. J. Earth Syst. Sci. 128, 123.

Hinze, W.J., von Frese, R.R.B., Saad, A.H. (2013). Gravity and Magnetic EXploration: Principles, Practices and Applications. Cambridge University Press, UK (512p).

Johnson, S.Y., Potter, C.J., Armentrout, J.M. (1994). Origin and evolution of the Seattle fault and Seattle basin, Washington. Geology 22, pp. 71–74.

Kaveh, A., Farhoudi, N. (2013). A new optimization method: dolphin echolocation. Adv. Eng. Softw. 59, pp. 53–70.

Karcıog˘lu, G., Gürer, A. (2019). Implementation and model uniqueness of particle swarm optimization method with a 2D smooth modeling approach for radio- Magnetotelluric data. J. Appl. Geophys. 169, pp. 37–48.

Kumar, C.R., Raj, A.S., Pathak, B., Maiti, S., Naganjaneyulu, K. (2020). High density crustal intrusive bodies beneath Shillong plateau and indo Burmese range of Northeast India revealed by gravity modeling and earthquake data. Phys. Earth Planet. Inter. 307, 106555.

Montesinos, F.G., Arnoso, J., Vieira, R. (2005). Using a genetic algorithm for 3-D inversion of gravity data in Fuerteventura (Canary Islands). Int. J. Earth Sci. 94, pp. 301–316.

Panisova, J., & Pasteka, R. (2009). The use of microgravity technique in archaeology: A case study from the St. Nicolas Church in Pukanec, Slovakia. Contributions to Geophysics and Geodesy, 39, pp. 237–254.

Parsopoulos, K.E., Vrahatis, M.N. (2002). Recent approaches to global optimization problems through particle swarm optimization. Nat. Comput. 1, pp. 235–306.

Rashedi, E., Nezamabadi, S., Saryazdi, S. (2009). GSA: a gravitational search algorithm. Inf. Sci. 179, pp. 2232–2248.

Rau, W.W., Johnson, S.Y. (1999). Well stratigraphy and correlations, western Washington and northwestern Oregon. U.S. Geol. Surv. Map Invest. pp. 1–36. I-2621, (3 sheets).

Rezaie, M. (2019). 3D non-smooth inversion of gravity data by zero order minimum entropy stabilizing functional. Phys. Earth Planet. Inter. 294, 106275.

Roshan, R., Singh, U.K. (2017). Inversion of residual gravity anomalies using tuned PSO. Geosci. Instrum. Method. Data Syst. 6, pp. 71–79.

Singh, A., Biswas, A. (2016). Application of global particle swarm optimization for inversion of residual gravity anomalies over geological bodies with idealized geometries. Nat. Resour. Res. 25, pp. 297–314.

Symons, N.P., Crosson, R.S. (1997). Seismic velocity structure of the Puget Sound region from three-dimensional non-linear tomography. Geophys. Res. Lett. 24, pp. 2593–2596.

Tarantola, A. (2005). Inverse Problem Theory and Methods for Model Parameter Estimation. Society for Industrial and Applied Mathematics (SIAM), Philadelphia.

Uwiduhaye, J.D., Mizunaga, H., Saibi, H. (2018). Geophysical investigation using gravity data in Kinigi geothermal field, Northwest Rwanda. J. Afr. Earth Sci. 139, pp. 184–19.